Dispersion-Free Quasi-Electrostatic Chip-Scale Floquet Topological Insulator for 5G Wireless Systems

Aravind Nagulu[1], Xiang Ni[2], Ahmed Kord[1], Mykhailo Tymchenko[3,4], Sasank Garikapati[1], Andrea Alù[2,4,5,*], and Harish Krishnaswamy[1*]

[1]*Department of Electrical Engineering, Columbia University, New York, NY 10027, USA*

[2]*Photonics Initiative, Advanced Science Research Center, City University of New York, New York, NY 10031, USA*

[3]*Lightmatter Inc., Boston, MA 02109, USA*

[4]*Department of Electrical and Computer Engineering, The University of Texas at Austin, Austin, TX 78712, USA*

[5]*Physics Program, Graduate Center, City University of New York, New York, NY 10026, USA*

[*]To whom correspondence should be addressed (email: harish@ee.columbia.edu, aalu@gc.cuny.edu)

Floquet topological insulators (TIs), whose exotic topological order is sustained by time-varying Hamiltonians, have been attracting significant interest in the condensed matter community. Their photonic analogues have been envisioned through spatio-temporal modulation of Hermitian systems, unveiling unique wave transport properties, with unique robustness and isolation features stemming from broken time-reversal symmetry. Given the challenges in generating and distributing modulation signals across an electrically large array with accurate phase synchronization, experimental realizations of Floquet TIs to

date have been limited to systems that emulate time with a spatial dimension, therefore preserving time-reversal symmetry and renouncing the most appealing feature of Floquet TIs – non-reciprocal topological protection. These limitations, combined with inherently narrowband responses, have so far prevented their applicability in real-life applications. In this paper, we unveil a new route to photonic Floquet TIs, based on quasi-electrostatic wave propagation in switched capacitor networks. This approach enables the first experimental demonstration of a non-reciprocal Floquet TI for electromagnetic waves, additionally offering an ultra-broad topological bandgap, spanning from DC up to GHz frequencies, within a deeply sub-wavelength form factor in a chip-scale integrated CMOS implementation. Our device operates beyond the delay-bandwidth (DBW) limit of conventional linear time-invariant electromagnetic structures by virtue of time modulation, and therefore offers extremely large delays despite the ultra-broad bandgap. Our design also features fine-grained reconfigurability, enabling robust and broadband signal routing and multiplexing functionalities. Our results bring the entire field of TIs to real-world applications, opening a path to the use of topological concepts in wireless communications, radar, quantum information processing and integrated photonics. As a demonstration, we have integrated our CMOS Floquet TI into 5G wireless systems, demonstrating multi-antenna full-duplex wireless operation and true-time-delay-based broadband beamforming enabled by its unique features of bandwidth, isolation, programmable nanosecond delays, extreme reconfigurability, and built-in strong robustness to defects.

1. Introduction

Topological insulators (TIs) are a recently discovered phase of matter, with an insulating response in the bulk, but acting as a conductor on the boundary[1-3]. Their conductive edge states are unidirectional and immune against reflections from surface imperfections or local disorder. These properties, originally discovered in the field of condensed-matter physics stemming from studies on the quantum Hall effect (QHE)[4], have been attracting significant interest from the broad scientific community for several years. Topological phenomena do not arise only in static systems, but also in periodically driven quantum systems, referred to as Floquet TIs, whose topological order stems from the external modulation[5-8]. Interestingly, the Chern number, commonly used to characterize the topological order in static TIs, is in some instances not sufficient to characterize the topological features of Floquet systems in their entirety, since anomalous chiral edge states may still arise when the Chern numbers of all Floquet bands are zero. In this situation, the topological order is encoded in the microscopic details of the driving protocol, rather than in the Floquet system itself[9,10].

In recent years, several works have been investigating new approaches to extend TI concepts from fermionic systems to classical photonics, electrical circuits[11-18], mechanics and acoustics[19-22], resulting in TIs for electromagnetic[23-35] and acoustic waves[36-42]. The underlying principles common to these works is the idea of inducing topological order either by breaking time-reversal symmetry (TRS) through magneto-optic phenomena or parametric modulation of the constituent elements, or by exploiting protected states arising from internal or spatial symmetries. The first approach has proven very effective to induce

strong topological robustness, since it breaks reciprocity and guarantees the absence of reflected edge states for any type of disorder[23,24,26,27,29,36,37,38,43]; on the contrary, symmetry-protected topological states are only immune against imperfections preserving the relevant symmetry[31,33,34,39,41,42], hence their robustness is inherently weaker. Periodically-driven spatio-temporal modulation can realize Floquet topological order, offering robust non-reciprocal topological protection. Reciprocity is broken through time modulation, hence avoiding the need of a magnetic bias, which offers great advantages for integration and practical implementations[27,36-38,43]. However, previous experimental implementations of Floquet TIs in photonics[29,44-46] have exclusively relied on replacing time with a relevant spatial dimension, resulting in arrays of evanescently-coupled optical waveguides slowly modulated in space along the direction of propagation. Clearly these systems do not explicitly break TRS, therefore they cannot offer isolation and strong topological protection. In addition, they are not feasible for on-chip implementation. Genuine Floquet TIs, on the contrary, require the generation and distribution of phase-synchronized time modulation signals across a large array[38,47,48], making their implementation challenging. Our recent experimental work showcasing an elastodynamic Floquet TI through a complex macroscopic network of separately-controlled piezo-electric resonators would be difficult to replicate over larger scales or in an integrated miniaturized design[43,48]. As an additional challenge, Floquet TIs typically exhibit a topologically-protected bandgap limited to a very narrow range of operating wavelengths, thus limiting their practical impact[29,38,40,44-46,49-51]. None of the recently proposed Floquet TIs have overcome these drawbacks, nor has a

realistic approach to address these limitations been put forward to the best of our knowledge.

In this paper, we present the first experimental demonstration of a Floquet TI for electromagnetic waves, i.e. a Floquet topological electromagnetic circuit or topolectric circuit, based on a completely new approach consisting of a network of quasi-electrostatic helicoidally-rotating elements[52]. The unit cells of our TI apply ultrabroadband synthetic rotation to the impinging signal in two dimensions, based on tailored spatio-temporal modulation of a switched-capacitor network supporting quasi-electrostatic signal propagation[53]. Compared to conventional approaches to TIs, which require a lattice period of the order of the wavelength to open a bandgap, hence leading to very large footprints, the rotation of each element is quasi-electrostatic in nature, fully relaxing this requirement and resulting in a deeply-subwavelength footprint for the entire Floquet lattice, and much easier phase-synchronized modulation. Furthermore, our quasi-electrostatic design results in a frequency-independent response, which supports a topological bandgap orders of magnitude more broadband than any previously reported photonic TI, extending from DC to GHz frequencies. The ultra-broad bandgap implies that it cannot be closed by small disorder, leading to high levels of robustness. At the same time, quasi-electrostatic wave propagation operates beyond the delay-bandwidth (DBW) limit of conventional linear time-invariant electromagnetic structures by virtue of time modulation[53], enabling our TI to offer extremely large delays despite the wide bandwidth. Each lattice node, being already modulated in time through commutated switches, may be dynamically reconfigured in real-

time to sustain a local handedness of choice, enabling the configuration of arbitrary routing of topologically-protected signals.

Our implementation offers a unique platform to probe the rich physics of topological wave propagation and to multiplex different functionalities for applications including wireless communications, radar and quantum information processing. We showcase its functionality in a 5G wireless system and an ultra-wideband impulse radar application. In the first scenario, the TI serves as a new antenna interface for a 750MHz full-duplex phased-array, in which the programmable delays within each lattice element enable independent phased-array beamforming in transmit- and receive-modes, and its isolation features enable full-duplex simultaneous transmission and reception of broadband radio-wave signals. The inherent reconfigurability of our TI enables the use of the same device as the antenna interface in an ultra-wideband true-time-delay (TTD) beamforming network for impulse radars, in which reconfigurable signal routing and wideband nanosecond-scale delays enable TTD-based beamforming of ultra-wideband signals spanning DC to GHz frequencies. In both cases, the achieved performance metrics exceed the current state of the art by several orders of magnitude, underscoring the utility of topological concepts in real-world applications. The topological features add intrinsic strong robustness of these functionalities to disorder and imperfections. These demonstrations truly open the field of TIs to real-world impact, exploiting their unique isolation and robustness, combined with broadband and seamless reconfigurability, to address the grand challenges of modern wireless systems.

2. Dispersion-Free Quasi-Electrostatic Reconfigurable Floquet TI

Floquet topological order is induced in our TI (Fig. 1(a)) by imparting distributed deeply subwavelength, broadband helicoidal rotation through a dense array of ultrabroadband circulators[52] arranged in a square lattice. Each circulator is realized based on the concept of quasi-electrostatic wave propagation in switched capacitor networks,[53] and consists of 8 identical switched-capacitor layers connected in parallel to 4 ports, as shown in the circuit diagram in Fig. 1(b). Each layer consists of a shunt capacitor connected to the 4 ports through transistor switches in a star configuration. A brief discussion on the operation of this element is included here, and the reader is directed to the supplementary material (section 1) for additional details. Switches across layers associated with a given port are modulated in a staggered fashion to turn them ON sequentially with no overlapping, and this scheme imparts a synthetic vertical-plane rotary motion that creates a quasi-electrostatic frequency-independent ring resonance within near-infinitesimal dimensions (see timing diagram in Fig. 1(b)). The switches within each layer are also modulated in a staggered fashion with no overlapping, imparting a synthetic horizontal-plane rotation that applies angular-momentum biasing[54] to break reciprocity. The overall result is a deeply-subwavelength element that effectively moves on a helicoidal path across layers, realizing *N*-port circulation over an extremely broad bandwidth within an infinitesimal footprint. In the case shown in Fig. 1(a), each element of the lattice supports wave propagation in the clockwise (CW) direction, i.e., from $T_1 \rightarrow T_2$, from $T_2 \rightarrow T_3$, and so on, providing isolation between any other pair of ports. Additionally, our CMOS chip implementation allows real-time reconfigurability of the modulation signal applied to the switches, enabling wide

reconfiguration of each element between CW handedness ($T_1 \rightarrow T_2 \rightarrow T_3 \rightarrow T_4$), counter-clockwise (CCW) handedness ($T_4 \rightarrow T_3 \rightarrow T_2 \rightarrow T_1$), and in general, other hybrid switching schemes, such as ($T_1 \rightarrow T_3 \rightarrow T_2 \rightarrow T_4$), ($T_1 \rightarrow T_4 \rightarrow T_3 \rightarrow T_2$). Fig. 1(c) shows the simulated scattering parameters of a 4-port, 8-layered circulator, modulated at f_m =500MHz. As shown in Fig. 1(d), the isolation mechanism in this unit cell architecture is due to charge-discharge through the port impedances, hence making this structure an extremely broadband alternative to previous time-modulated implementations of non-reciprocal angular-momentum devices,[54,56] which rely on destructive interference of the signal coming through two different paths or modes. Additionally, its infinitesimal form-factor is 100-1000× more compact than architectures based on resonators[54,56].

Floquet TI: We take advantage of this synthetic helicoidal rotation and broadband non-reciprocal response at the unit cell level to implement a chip-scale Floquet TI by connecting these elements in a 4x4 square lattice, and driving them through a common modulation clocking circuitry, as shown in Fig. 1(a). When all the unit cells are configured with the appropriate handedness, the signal propagation through this lattice is analogous to the transport of an electron traveling through a two-dimensional lattice with magnetic bias applied on each atom, in which the role of magnetic bias is replaced by the angular momentum imparted by each unit cell. Hence, we expect the lattice to exhibit topological features, analogous to those envisioned in Ref. 38, but here extended over an extremely broad bandwidth and within an ultra-compact, resonator-free form factor. We will determine more rigorously the topological features of this helicoidally-rotating lattice in the next section. Small inductive coupling elements between the unit cells have been added

to enhance the non-reciprocal performance of the individual units[52] by enabling complete energy transfer between neighboring elements[52], which is equivalent to complete charge transfer from one shunt capacitor to the next. Using wideband, resonator-free elements relaxes the component mismatch requirements, and it alleviates fabrication and layout challenges of an electrically-large lattice of high-Q resonators, as in all previous designs for Floquet TIs[27,36,38,48].

While the deeply-subwavelength dimensions of the lattice ease the modulation signal distribution, Floquet TIs are inherently prone to phase desynchronization of the modulation signal and harmonic conversion phenomena. On the contrary, our TI implementation, as described in the supplementary material (section 1C), offers substantial resilience to modulation clock phase deviations (up to ±12.5% of the time period T_m in our implementation).

3. Network Theory for Floquet TIs Based on Resonator-Free Lattices

The lattice elements in our TI are quasi-electrostatic in nature, and hence support dispersion-free nonreciprocal signal propagation. Therefore, the conventional coupled mode theory based on resonant modes cannot accurately describe our system. To rigorously demonstrate the topological features of our quasi-electrostatic lattice and the emergence of topological edge states with ultrabroad bandwidth, we turn to resonator-free Floquet network theory, which was initially introduced to explain the integer QHEs[57], and used in later efforts to investigate the Floquet topological properties of strongly-coupled resonators[58-60]. The Floquet network model usually deals with two-port scatterers, while

the elements of our chip-scale Floquet TI consist of four-port circulators, whose scattering equations are

$$b_j = s_{j,i}a_i, i, j = 1,2,3,4, \tag{1}$$

where $s_{j,i}$ is the scattering coefficient of a four-port circulator, $i, j = 1,2,3,4$ are cyclic indices, and a_i and b_j are ingoing and outgoing signals, respectively. The scattering parameters are constrained by rotational symmetry, such that $s_{j,i} = s_{j+1,i+1}$. To facilitate the analysis, we provide a specific choice regarding the plaquette of the network lattice, around which the field travels either in a CW pattern or CCW pattern, corresponding to CW modes and CCW modes, respectively. Therefore, we can treat the scattering process of the four-port circulators arranged in the network lattice as the separate scattering processes of CW modes (pseudo spin up) and CCW modes (pseudo spin down) and the mixed scattering processes (pseudo spin couplings) between them. Notice that the choice of plaquette is arbitrary and will not alter the end result. Without loss of generality, we rearrange the scattering equations in (1) according to the plaquette shown in Fig. 2(a) as follow

$$\begin{pmatrix} B_{\mathrm{cw}} \\ B_{\mathrm{ccw}} \end{pmatrix} = \begin{pmatrix} S_{\mathrm{cw}} & S_{\mathrm{int}} \\ S'_{\mathrm{int}} & S_{\mathrm{ccw}} \end{pmatrix} \begin{pmatrix} A_{\mathrm{cw}} \\ A_{\mathrm{ccw}} \end{pmatrix}, \tag{2}$$

where the CW and CCW propagating fields at incoming (outgoing) ports are represented by $A(B)_{\mathrm{cw}} = [a_1(b_4), a_3(b_2)]^{\mathrm{T}}$ and $A(B)_{\mathrm{ccw}} = [a_2(b_3), a_4(b_1)]^{\mathrm{T}}$, respectively. $S_{\mathrm{cw(ccw)}}$, S_{int} and S'_{int} are taken from Eq. (1), and S_{int} (S'_{int}) couples CW modes and CCW modes. When the circulator is synthetically rotated with CW handedness, for example $|s_{i+1,i}| > |s_{i+2,i}| > |s_{i+3,i}|$, the four-port scattering is equivalent to the superposition of

strong coupling of CCW modes, weak coupling of CW modes, as well as negligible mixing of CW and CCW modes in the two-port network models (Fig. 2(a)). As a consequence, the dynamics of the CW mode family map to those of the well-known Floquet two-port network model, which support anomalous topological phase and topological edge states under the strong scattering condition[59]. Meanwhile, the dynamics of the CCW modes map to a topologically trivial phase because of the weak scattering, and the interaction between CW modes and CCW modes is too weak to have a determining effect on the topology of the respective subspaces. The spatio-temporally-modulated angular-momentum (STM-AM) bias applied to each lattice element guarantees that the strong scattering condition $|s_{i+1,i}| \gg |s_{j,i}|, j \neq i+1$ is met over a wide bandwidth that extends from DC to GHz frequencies, ensuring that our quasi-electrostatic system possesses dispersion-free nontrivial topology in the ideal case.

To demonstrate the existence of broadband topological edge states supported by our system, we construct the supercell network of the square lattice formed by the four-port circulators, which is periodic in the *x* direction and has a finite length *L* in the *y* direction. According to the relation between the fields of each four-port circulator and the fields of two-port scatterers via Eq. (2), as well as the boundary conditions in the network lattice, the governing equations can be found as (see section 2 of the supplementary material for details)

$$\widehat{H}_F(\phi)\psi = e^{-ik_x}\psi, \tag{3}$$

where ψ is composed of fields at port 1 and port 2, and ϕ is the phase delay when the field propagates from one port to the next. Since Eq. (3) resembles the Floquet eigenvalue

equations of a periodically driven system[9], $\widehat{H}_F(\phi)$ can be treated as a Floquet Hamiltonian, and k_x is the projected momentum vector in the x direction, and phase ϕ plays the role of quasienergy. The scattering components $s_{j,i}$ in our quasi-electrostatic system can be approximately modelled as

$$
\begin{aligned}
s_{i+1,i} &\approx \left[1 - 0.5\left(e^{-2\frac{T_m}{NZ_0C}} + e^{-4\frac{T_m}{NZ_0C}}\right)\right] e^{-\mathrm{i}\omega_{in}\frac{T_m}{4}}, \\
s_{j,i} &\approx e^{-\{(j-i-1)\%L\}\frac{T_m}{NZ_0C}}\, e^{-\mathrm{i}\{(j-i)\%L\}\omega_{in}\frac{T_m}{4}}, j \neq i, i+1, \\
s_{i,i} &\approx 0,
\end{aligned}
\tag{4}
$$

where ω_{in} is the input frequency, Z_0 is the port impedance, N=8 is the number of layers in the unit circulator, C is the shunt capacitance of each layer, $T_m = 1/f_m$, L=4 is the number of ports in the circulator, and % represents the modulo operation (see section 1A of the supplementary material for details on this modeling). In our experiments, the parameter $\frac{T_m}{NZ_0C} = 2$, leading to strong scattering of CCW modes. Using the scattering parameters in Eq. (4), we obtain the Floquet band structure of the supercell network shown in Fig. 2(b). Interestingly, we observe flat bands (shown as red lines) stemming from bulk modes arising from the trapped resonance in the plaquette of the network lattice when the phase delay meets the condition $\omega_{in}T_m = 2\pi q,\ q = 0,1,2..$, or equivalently $f_{in}/f_m = q$, i.e., at operating frequencies that are multiples of the modulation frequency. In addition to these bulk bands, linear edge bands (blue lines in Fig. 2(b)) arise across the whole band structure. Since f_{in} is linearly proportional to the transmission phase which is in-turn periodic, topological edge bands are continuously extended in the frequency dimension, as

long as the strong scattering condition, or equivalently, the strong circulation condition implemented in the experiment, is satisfied. Depending on the phase delay of the signal at the boundaries, topological edge states may have different group velocities from the one shown in Fig. 2(b), and more details are provided in the supplementary materials (section 3) with respect to this property.

To further reveal the broadband features of the topological edge states and the existence of bulk states, we carried out simulations of a finite network consisting of a 10×10 array. In order to emulate grounded boundary conditions at the border of the electrical circuit, the outgoing fields at the bottom and right edges are enforced to be zero. In the first example, the input port is placed at the left bottom site of the lattice, and f_{in} is swept from 0 to $2f_m$. The transmittance spectra as a function of f_{in} are produced from data taken in the bulk regions (indicated by dashed boxes in Fig. 2(d)). As shown in Fig. 2(c), the transmittance is significantly larger near bulk frequencies ($f_{in}/f_m = q$) than at other frequencies, indicating that the fields are concentrated at the edges and dissipate inside the bulk of the lattice at arbitrary frequencies except at bulk frequencies. Furthermore, by plotting the field distribution of the lattice (Fig. 2(d)), we observe that the excited fields are mostly concentrated at the right and top edges of the lattice for arbitrary f_{in} except at and near $f_{in}/f_m = q$. Throughout all this frequency range, we observe signal transport in a CW rotating pattern, stopping at the right top corner due to the grounded boundary condition (see for example left and right panels in Fig. 2(d)). This ultra-broadband feature arises from the linearly extended edge bands in the frequency dimension presented in Fig. 2(b). The middle panel in Fig. 2(d) shows the field distribution for $f_{in} = 0.95f_m$: besides the

excitation of edge modes, both CW and CCW bulk modes are excited, and all lattice elements have nonzero fields. Unlike topological edge states, topologically-trivial circulating modes would be independent of the input frequency and the excited fields would always localize at edges. In the second example in Fig. 2(e), the input port is changed to the top right site of the lattice. Due to the anomalous topological phase of the system, the network only supports chiral edge states propagating in a CW rotating pattern. As a result, the fields are absorbed immediately by the right boundaries, as they propagate downward, and no field is backscattered because of the topological protection. This phenomenon is totally independent of f_{in}, except at and near $f_{in}/f_m = q$ when bulk modes arise (middle panel in Fig. 2(e)). In the supplementary material (section 3), we study the network lattice formed by two-port scatterers under the strong scattering condition, showing that it possesses the same topological order as our array. We emphasize that the Chern numbers of all flat Floquet bands are zero; the nontrivial topology here arises from the strong scattering of the network lattice achieved by the CW rotation of the unit cell elements[58]. In the supplementary materials (section 4), we have carried out first-principle circuit simulations of a 900-element lattice (30×30), and the results closely match both our theoretical model and our experimental results.

In addition to the resonant-free network model, we also carried out Floquet coupled mode analysis for square lattices based on STM-AM biased LC-resonator unit cells, where the role of the magnetic bias is replaced by the synthetic rotation imparted by temporal modulation, as rigorously shown in the supplementary material (section 3). This analysis showcases the physics of our system, mapping our frequency-independent response to the

center of the relevant bandgap in this resonant lattice. Furthermore, the LC-resonator-based Floquet TI stands in contrast to our quasi-electrostatic TI in that it exhibits far more dispersion and a far narrower bandgap, underscoring the benefits of our approach.

4. Experimental Results

Having determined that our lattice supports Floquet topological features over an ultra-broadband frequency range, we have implemented a 45nm SOI CMOS chip realizing the first photonic Floquet TI. Fig. 1(a) shows the microphotograph of our deeply-subwavelength chip-scale quasi-electrostatic Floquet TI, with a size of 3.5mm×3.4mm (~λ/860×λ/880 at 100MHz and ~λ/86×λ/88 at 1GHz). By changing the switching scheme, the lattice topology can be dynamically reconfigured locally, namely, the nontrivial topological subspace can be switched between CW-mode and CCW-mode families, corresponding to opposite chirality of edge states when all the unit cells are configured for CW/CCW handedness, to create propagation along arbitrarily-shaped domain walls between sub-lattices with varied topologies, and even to support bulk transmission if we implement the hybrid modality in each node. These functionalities are experimentally validated below, along with the utility of this TI in 5G wireless and ultra-wideband impulse radar applications.

Unidirectional Edge States with Topological Protection: When the lattice elements are configured for CW rotation and modulated at f_m=500MHz, the lattice exhibits an overall anomalous topological phase, and it does not support any bulk mode except at and near $f_{in} = qf_m$, as predicted by our Floquet network theory and verified by the experimental

results shown in Fig. 3. Indeed, the measured transmission spectra for CW propagation along the edge (top left panel in Fig. 3(a)) are significantly larger than those for CCW propagation (top right). The isolation accumulates along the edge in the CCW direction, increasing at a rate of ~20dB per element until it reaches the chip-level parasitic limit of 60-70dB. We note that such a high level of isolation cannot be achieved in a single circulator unit cell without the use of tuning elements and real-time configuration over a narrow bandwidth, due to fabrication tolerances and impedance mismatches, and it can never be achieved in a single element over such a wide bandwidth. The group delay linearly increases for CW propagation along the edge as expected (bottom left panel of Fig. 3(a)), which provides additional evidence of the emergence of topological edge states. The emergence of bulk modes is evident both in first-principle simulations of the electrical circuit (see section 4 of the supplementary material) and in our experimental results shown in Fig. 3(b), in which the transmittance of bulk nodes exhibits peaks near $f_{in} = 0$ and $f_{in} = f_m$.

The ultra-broadband, dispersion-free operation of our Floquet TI is illustrated through field distributions plotted at different signal frequencies, such as $f_{in} = 0.5f_m$ and $1.6f_m$, as shown in Figs. 4(a) and (b). When the signal is excited at P_{16}, the signal travels along the edge to P_8 in CW direction while reflecting off of the ports with open termination (P_1 through P_7) and not propagating in the bulk as shown both in the left and right panels of Fig. 4(a). When the frequency of the signal is chosen as $f_{in} = f_m$, the signal power decays more slowly and spreads over a larger area of the lattice when compared to the previous cases, indicating the bulk states are excited as well (middle panel of Fig. 4(a)). On the other

hand, when the signal is excited at P_8, it continues to travel in the CW direction and is dissipated into the absorptive terminations at ports P_9 through P_{15}, and no backscattering signal at P_{16} is detected due to the topological prohibition of backward states as shown in Fig. 4(b). The middle panel in Fig. 4(b) shows the more diffusive spread of the signal compared to the left and right panels, which further verifies the fact the bulk states are excited. Thus, the strong contrast between CW and CCW rotation in Fig. 4(a,b) validates the claim of anomalous topological phase of the Floquet TI and confirms our theoretical model. Similarly, the lattice can be dynamically reconfigured to the nontrivial topology of the opposite mode family by reversing the handedness of synthetic rotation of each unit cell.

The operational bandwidth of a system should be evaluated in comparison to the central frequency of operation, defining the $\text{Fractional Bandwidth} = \frac{\text{Signal Bandwith}}{\text{Center Frequency}} \times 100\%$. In this context, it is particularly challenging to achieve broadband operation from extremely low frequencies (near-DC) to high frequencies due to the wide disparity in wavelength/frequency. A circuit that operates from DC to GHz frequencies, as the one presented here, achieves a Fractional Bandwidth of 200%, which is the maximum achievable value. The topological features of our circuit offer orders of magnitude larger fractional bandwidth than any other time-invariant and/or time-variant photonic TI (Fig. 3(c)). For instance, the TI in Ref. 24 achieves topological edge protection across a bandwidth of 0.27GHz while operating around 4.485GHz, leading to a fractional bandwidth of ~ 6%. Similarly, in Ref. 61, topological protection is demonstrated over

<0.3GHz while operating around a center frequency of 7.75GHz, thereby leading to a fractional bandwidth of ~ 3.8%. Finally, in Ref. 38, the acoustic Floquet TI proposed achieves topological protection over ~0.5KHz while operating around a center frequency of ~22KHz, thereby leading to a fractional bandwidth of ~ 2.2%. On the other hand, our experiment demonstrates wideband topological protection, ranging from DC to 1GHz, with a fractional bandwidth of 200%. Interestingly, the upper frequency limit is only determined by the specific switching technology at hand, and it may be further extended using different CMOS platforms.

Robustness to Defects and Lattice Disorder: A topological edge mode in a non-reciprocal Floquet TI is immune to lattice disorder and defects, since the absence of backward edge and bulk modes ensures no reflections and no scattering. In our experiments, this topological robustness is confirmed by artificially inducing a drastic defect, i.e., turning OFF one of the lattice nodes along the edge, as shown in Fig. 5(a). In contrast to the topologically trivial lattice, the signal propagation in our Floquet TI is unaffected even in the absence of one of the nodes due the topological nature of the lattice. As noticed through the field distributions, the signal travels around the defect (signal path in Fig. 5(a)), thus preserving the anomalous topological phase and isolation across the bulk. Transmission across the defect results in a longer transmission path, as evidenced by the increase in group delay shown in Fig. 5(b).

Reflection-less Domain Walls with Arbitrary Shape: In addition to robustness against defects, our reconfigurable Floquet TI can also create reflection-less tailored domain walls of arbitrary shape, thus providing significant control over wave propagation and

multiplexing opportunities. For instance, Fig. 5(c) shows a tailored domain-wall boundary created between any two points, with arbitrary shape, by reversing the propagation direction of the elements on one side of the boundary. The signal propagates robustly along the domain wall without penetrating into the bulk on either side.

5G Wireless Full-Duplex Phased Array Applications: The wide bandwidth, reconfigurable signal routing, non-reciprocal isolation, wideband nanosecond-scale delays, and robustness to defects offered by our Floquet TI platform, along with its implementation in a CMOS chip, open a plethora of real-world applications in wireless communications, radar, and quantum information processing.

Full-duplex wireless is an emerging wireless communication paradigm in which the transmitter and receiver operate at the same time and at the same frequency, thus doubling the network capacity compared to conventional time-division and frequency-division duplex wireless[62-64]. In order to combat the inherently-large self-interference from the transmitter to the receiver, non-reciprocal circulators[52,56,65-66], RF/analog cancellers[64] and digital cancellers[62] have been investigated. In this context, combining full-duplex operation with multi-antenna technology, such as phased arrays[67] and MIMO transceivers[68], can exploit their combined benefits, but the self-interference is enhanced to the order of $O(M^2)$, where M is the number of antennas[68]. The properties of our CMOS Floquet TI are ideally suited to address this challenge and support a multi-antenna interface for full-duplex phased-array transceivers, enabling phased-array beamforming for the transmitter and receiver arrays while maintaining large isolation between the two. A full-duplex phased-array experiment involving our CMOS TI is shown in Fig. 6(a), where 4 transmitters,

receivers and patch antennas operating at 730MHz are interfaced with the Floquet TI modulated at 500MHz. By programming the clock delays within each lattice element, programmable delays of $2f_m/8$-$9f_m/8$, or entire 360° phase shifting at frequencies > f_m, are introduced between each transmitter/receiver and its antenna, allowing for complete, simultaneous and independent transmitter/receiver beamforming. The TI at the same time ensures isolation between every transmitter-receiver pair. Measured phased-array beam patterns for the transmitter and receiver arrays are shown in Fig. 6(b) for normal, +45° and -45° steering. With the transmitter and receiver arrays configured for +45° and 0° steering, respectively, the overall array isolation measured from the transmitter power splitter input to the receiver power combiner output (calibrating out the losses of the splitter and combiner) is +44.1dB (see Fig. 6(c)), enabling the simultaneous reception of a +10dBm continuous-wave signal transmitted from a dipole antenna 6m away with ~0dB signal-to-interference/noise-ratio (SINR). When compared with state-of-the-art multi-antenna full-duplex systems[67,68], which achieve ~15dB TX-to-RX isolation at the antenna interface, our prototype achieves up to 30dB higher isolation, thereby greatly relaxing the dynamic-range requirements of the subsequent receiver. Introducing additional 50dB of self-interference cancellation using conventional RF/analog and digital techniques can enable 600m link range at 10dB SINR assuming traditional Friis transmission path loss, thus showcasing the powerful impact of our CMOS TI as a programmable multi-antenna interface for full-duplex phased-array wireless systems.

Ultra-wideband True-Time-Delay Beamforming for Impulse Radar: Ultra-wideband (UWB) impulse radars operating over bandwidths spanning DC to GHz frequencies find

application in indoor object detection, positioning and tracking due to their benefits of high precision, and penetration through large objects and walls[69,70]. Beam-steering across multiple antennas over such wide bandwidths requires wideband, true-time delays (TTDs), but the nanosecond-scale delays required by these radar systems for beam steering functionality have been beyond reach in IC implementations, due their large form factor and high insertion loss[70]. Again, our dispersion-free CMOS Floquet TI offers unique features in terms of reconfigurable signal routing with programmable wideband nanosecond-scale delays, ideally suited to support TTD beamforming across multiple antennas and transmitters/receivers, as shown in Fig. 7(a) for a system with 8 elements. Each antenna-receiver pair consists of two circulator elements in the signal path, where one element is operated in clockwise/counter-clockwise mode and can offer its entire delay coverage ranging from $T_m/8$ – $7T_m/8$, while the other element is operated in a hybrid configuration, i.e., $T_1 \rightarrow T_3 \rightarrow T_2 \rightarrow T_4$, and is shared across two antenna-receive pairs, resulting in delays ranging from $T_m/8$ – $3T_m/8$ for each pair. Therefore, a modulation frequency of 500MHz leads to a programmable delay in each antenna-receiver pair ranging from 500ps to 2.5 ns with a -3dB bandwidth of 1.25GHz.

It should be noted that the quasi-electrostatic wave propagation supported by our Floquet TI operates well beyond the delay-bandwidth product trade-off of conventional linear time-invariant electromagnetic structures[53], and it surpasses this bound by virtue of its time-varying features. For example, as we show in Supplementary Fig. 4 (c-e), if the time modulation (represented by phase delay ϕ) for the elements in the bulk are fixed, while phase delay ϕ' at the boundaries are varied from ϕ to $2\,\phi$ and to $10\,\phi$, the topological

edge states wind in the bandgap with a different slope, while the overall bandwidth of the topological bandgap stays the same, and thus the delay-bandwidth (*DBW*) product increases proportionally with the winding number of the topological edge states. This is remarkably different from conventional photonic TIs, which experience a drastic trade-off between the bandgap opening and the achievable delay sustained by edge states. In our platform, the maximum delay imparted by a single unit cell is approximately equal to the clocking time period ($\frac{N-1}{N}Ts \sim T_s$ for large N) and the signal bandwidth is proportional to the number of parallel layers (N) times the clocking frequency (f_s) (-3 dB bandwidth ~ $0.375Nf_s$). This leads to a *DBW* product that is proportional to the number of parallel layers (N) in the unit cell (*DBW ~ 0.375×(N-1)*). Implementing a device with a larger number of parallel layers increases the delay-bandwidth product, and largely overcomes the delay-bandwidth trade-off conventionally seen in time-invariant electromagnetic structures[53] and in all previous photonic TI demonstrations. For reference, the unit cells of our lattice are implemented using 8 parallel paths, imparting a maximum delay of 1.75ns with a -3dB bandwidth of 1.4GHz. Therefore, our experimentally demonstrated delay-bandwidth product is 2.45, which is close to the theoretical delay-bandwidth product of an 8-path unit element (theoretical *DBW* = 0.375×7 = 2.62).

True-time-delay systems are typically characterized using two metrics, (i) the delay-bandwidth-miniaturization-factor product, and (ii) the noise figure, to evaluate noise performance. Passive delays based on transmission lines or miniaturized LC delays[71,72] exhibit low delay-bandwidth-miniaturization product, since they are limited by the DBW trade-off of linear time-invariant systems and tend to be large in size, while delay elements

based on active current/voltage-biased transistors[73] suffer from poor noise and linearity performance. Our Floquet TI lattice, in contrast, exhibits a delay-bandwidth-miniaturization product that is several orders of magnitude larger than passive implementations, and lower noise figure when compared with active implementations. For instance, prior passive true-time-delay proposals that rely on quasi-distributed LC networks in Ref. 71 (Ref. 72) can impart a maximum delay of 400ps (180ps) across a -3dB bandwidth of 13GHz (7.6GHz) while occupying an chip area of 2.5mm^2 (1mm^2) , i.e., a miniaturization factor (λ_{center}^2/Area) of 4×10^2 (2×10^3), thereby resulting in a delay-bandwidth-miniaturization-factor product of 2×10^3 (2.7×10^3). In comparison, our prototype can impart a maximum delay of 2.5ns over a -3dB bandwidth of 1.25GHz while occupying a chip area of 1.5mm^2 per channel (i.e., miniaturization factor of 2.4×10^5), resulting in a delay-bandwidth-miniaturization-factor product of 7.5×10^5, which is 10^2-$10^3\times$ higher when compared with prior passive proposals. On the other hand, the prior active delay implementation in Ref. 73 can also achieve a comparable delay-bandwidth-miniaturization-factor product, but it exhibits a large noise figure of 17.5-23dB. In comparison, our prototype achieves a noise figure of 6-9dB which is up to 12dB or 15.8× lower, thereby significantly advancing the state of the art in true-time-delay system performance.

Fig. 7(b) shows a time domain simulation obtained using the measured scattering parameters of our Floquet TI for a 1×8 antenna array with a free-space path distance of 12cm between two consecutive antennas. Here, a UWB mono-pulse radar signal[69] with a carrier frequency of 730MHz and a -3dB bandwidth of 830MHz is time-shifted and

incident on the antenna ports to emulate a -40^{o} angle of arrival. The Floquet TI compensates for the delay-difference between the antennas and enables constructive summation across all the receiver ports, as shown in Fig. 7(b). In the presence of a defect, which is artificially induced by turning off switches in the 5th beamforming path (ANT_5 – RX_5), the signal travels around the defect due to the topological robustness, thereby preserving signal propagation and beamforming capabilities. Figs. 7(a) and (b) also depict the transmission path and the output signals at the RX ports in the presence of a defect in the 5th beamforming path. Adjusting the delays in the unit cells enables achieving the desired delay despite the longer transmission path. A longer path can lead to higher transmission loss which can be easily compensated through amplitude/gain control, which is straightforward to implement in beamformers[70]. Through our programmable delays, the beam pattern of such a 1×8 UWB array can be steered from +40^{o} to -40^{o}, and the synthesized array gain patterns, sans the defect, based on measured scattering parameters for normal, +40^{o} and -40^{o} steering directions, are shown in Fig. 7(c).

5. Conclusions

In this paper, we presented the first experimental realization of a nonreciprocal photonic Floquet TI, and demonstrated its impact in practical 5G wireless system demonstrations. Our implementation overcomes two fundamental challenges of conventional photonic TIs: it is orders of magnitude broader bandwidth than any photonic TI implemented to date, and it fits within an extremely compact, deeply subwavelength, form factor, which overcomes challenges associated with distribution of the modulation signal and allows its integration into a CMOS chip.

The topological nature of our circuit has been theoretically verified by a generalization of Floquet network theory to arrays of four-port circulators. The quasi-electrostatic nature of our circuit results in deeply-subwavelength dimensions and in a dispersion-free bandgap extending from DC to GHz frequencies. Our integrated CMOS implementation of the Floquet TI leverages a novel interface modulation technique to realize an electrically-large Floquet TI with resilience to modulation clock phase deviations across the lattice. Our experiments validate the unidirectional topologically-robust properties of edge modes and other topological features of the lattice, such as robustness to defects and lattice imperfections. We further discussed the wide-range of reconfigurability available within the implemented Floquet TI, such as the ability to create artificial boundaries in the bulk by splitting it into two domains with opposite spins.

These results open the door to numerous practical applications of reconfigurable TIs as reciprocal/non-reciprocal signal multiplexers for wireless communication systems, radar and quantum information processing systems. Two experiments were conducted to demonstrate the practical relevance of our Floquet TI as an inherently robust and highly reconfigurable antenna interface for 5G full-duplex phased-array wireless and ultra-wideband impulse-radar beamforming applications. Similar operations can be envisioned to interface a multitude of qubits to excitation and readout circuitry in quantum computing applications.

A related work was recently published in [ref], in which anomalous topological edge states were observed in a lattice of magnetic circulators, highlighting their superior robustness over Chern type edge states, consistent with the conclusions in our paper. We

stress that our paper describes a chip-scale implementation based on switched-capacitor circulators, which do not require a magnetic bias and achieve ultra-wide bandwidths, along with experimental demonstrations in emerging 5G applications, namely full-duplex phased arrays and ultra-wideband true-time-delay arrays for impulse radar.

Methods

CMOS Implementation. As mentioned earlier, our 45nm SOI CMOS dispersion-free photonic Floquet TI is implemented as a lattice of 4×4 helicoidally-rotating quasi-electrostatic circulator unit cells. Each layer of the 4-port, 8-layered unit circulator consists of a 2.5pF shunt capacitor connected to 4 ports through 50μm/40nm transistor switches. The ON-resistance of these transistor switches is ~5.6Ω. The coupling inductors between the unit circulators are implemented on chip using 4-turn lumped inductors with stacked metal layers to achieve compact area and low resistive losses. The bulk nodes of our Floquet TI are connected to unity gain buffers whose outputs are multiplexed to a pad for measurement of the field distributions presented in Figs. 4 and 5. The clocking circuitry consists of pseudo-differential buffers to generate square-waves from the input 2GHz differential sinusoidal signals. These 2GHz square wave signals were divided by a factor of 4 and then fed to a non-overlapping clock-generator to generate the 8 phases of 500MHz, 12.5% duty cycle non-overlapping clocks that drive the switches in the circulators.

Discussion of Loss Effects. A critical parameter that governs practical applicability is the insertion loss. A single circulator element within the lattice exhibits a transmission loss of 4-5.5dB to the next port, isolation of 15-20dB to the following port, and 25-35dB to the subsequent ports (Fig. 3(a)). Of this 4-4.5dB of loss, harmonic conversion loss contributes

~1-1.5dB and the remaining ~3-3.5dB arises from parasitic contributors. As the signal propagates through multiple elements, the parasitic contributions accumulate, while the contribution of harmonic conversion losses does not increase (see section 1B and section 4 of the supplementary information). It should be noted that the parasitic loss of 3-3.5dB per unit cell can be reduced through the use of scaled CMOS technology nodes that offer transistors with reduced ON resistance and parasitic capacitance. In the limit, as the contribution of these parasitic losses becomes negligible, the loss from harmonic conversion is the only contributor, and it improves with the number of parallel layers *N*. Hence, ideally, a lattice of arbitrarily large size can be realized with low insertion loss of ~1-1.5dB (corresponding to the harmonic conversion loss of a single element) as CMOS technology scales.

5G Wireless Full-Duplex Phased Array Experiment. The measurement setup for the full-duplex phased-array experiment involving our CMOS TI is shown in Fig. 6(a), where 4 transmitters, receivers and patch antennas operating at 730MHz are interfaced with the Floquet TI modulated at 500MHz. The 4 transmitter ports are fed from a universal software radio peripheral (USRP) generating a +11dBm, 20MHz, OFDM-QPSK signal that is power-split 4 ways, resulting in +0.4dBm incident on each transmitter port (total power of +6.4dBm across 4 elements), while the 4 receiver ports are combined and monitored on a spectrum analyzer.

Data Availability

The authors declare that all relevant data are included in the paper and the Supplementary Information. Additional data are available from the corresponding authors upon request.

Acknowledgements

This work was supported by the DARPA SPAR program, the AFOSR MURI program, the Office of Naval Research, and the Department of Defense. Xiang Ni thanks Yugui Peng for the helpful discussion.

Author Information

These authors contributed equally: Aravind Nagulu, Xiang Ni and Ahmed Kord.

References

1. Hasan, M. Z. & Kane, C. L. Colloquium: Topological insulators. *Rev. Mod. Phys.* **82**, 3045-3067 (2010).
2. Qi, X. L. & Zhang, S. C. Topological insulators and superconductors. *Rev. Mod. Phys.* **83**, 1057-1110 (2011).
3. Moore, J. E. The birth of topological insulators. *Nature* **464**, 194-198 (2010).
4. Thouless, D. J., Kohmoto, M., Nightingale, M. P. & Dennijs, M. Quantized Hall Conductance in a Two-Dimensional Periodic Potential. *Phys. Rev. Lett.* **49**, 405-408 (1982).
5. Kitagawa, T., Berg, E., Rudner, M. & Demler, E. Topological characterization of periodically driven quantum systems. *Phys. Rev. B* **82** (2010).
6. Lindner, N. H., Refael, G. & Galitski, V. Floquet topological insulator in semiconductor quantum wells. *Nat. Phys.* **7**, 490-495 (2011).
7. Katan, Y. T. & Podolsky. D. Modulated Floquet Topological Insulator. *Phys. Rev. Lett.* **110**, 016802 (2013).
8. Cayssol, J., Dóra, B., Simon, F. & Moessner, R. Floquet topological insulators, *Phys. Status. Solidi RRL* **7**, 101–108 (2013).
9. Rudner, M. S., Lindner, N. H., Berg, E. & Levin, M. Anomalous Edge States and the Bulk-Edge Correspondence for Periodically Driven Two-Dimensional Systems. *Phys. Rev. X* **3** (2013).
10. Nathan, F. & Rudner, M. Topological singularities and the general clasification of Floquet-Bloch Systems. *New J. Phys.* **17**, 125014 (2015).

11. Albert, V.V., Glazman, L. & Jiang, L. Topological Properties of Linear Circuit Lattices. *Phys. Rev. Lett.* **114,** 173902 (2015).
12. Ningyuan, J., Owens, C., Sommer, A., Schuster, D. & Simon, J. Time- and Site-Resolved Dynamics in a Topological Circuit. *Phys. Rev. X* **5,** 021031(2015).
13. Imhof, S., Berger, C., Bayer, F., Brehm, J., Molenkamp, L.W., Kiessling, T.*, et al.* Topolectrical-circuit realization of topological corner modes. *Nat. Phys.* **14**, 925–929 (2018).
14. Serra-Garcia, M., Susstrunk, R. & Huber, S.D. Observation of quadrupole transitions and edge mode topology in an LC circuit network. *Phys. Rev. B,* **99**, 020304(R) (2019).
15. Hofmann, T., Helbig, T., Lee, C.H., Greiter, M. & Thomale, R. Chiral Voltage Propagation and Calibration in a Topolectrical Chern Circuit. *Phys. Rev. Lett.* **122**, 247702 (2019).
16. Bao, J.C., Zou, D.Y., Zhang, W.X., He, W.J., Sun, H.J. & Zhang, X.D. Topoelectrical circuit octupole insulator with topologically protected corner states. *Phys. Rev. B* **100**, 201406(R) (2019).
17. Ni, X., Xiao, Z.C., Khanikaev, A.B. & Alu, A. Robust Multiplexing with Topolectrical Higher-Order Chern Insulators. *Phys. Rev. Appl.* **13**, 064031 (2020).
18. Wang, Y., Price, H.M., Zhang, B.L. & Chong, Y.D. Circuit implementation of a four-dimensional topological insulator. *Nat. Commun.* **11**, 2356 (2020).
19. Lu, L., Joannopoulos, J. D. & Soljaclc, M. Topological photonics. *Nat. Photonics* **8**, 821-829 (2014).
20. Khanikaev, A. B. & Shvets, G. Two-dimensional topological photonics. *Nat. Photonics* **11**, 763-773 (2017).
21. Ozawa, T. *et al.* Topological photonics. *Rev. Mod. Phys.* **91**, 015006 (2019).
22. Ma, G. C., Xiao, M. & Chan, C. T. Topological phases in acoustic and mechanical systems. *Nat. Rev. Phys.* **1**, 281-294 (2019).
23. Haldane, F. D. M. & Raghu, S. Possible realization of directional optical waveguides in photonic crystals with broken time-reversal symmetry. *Phys. Rev. Lett.* **100**, 013904 (2008).
24. Wang, Z., Chong, Y. D., Joannopoulos, J. D. & Soljacic, M. Observation of unidirectional backscattering-immune topological electromagnetic states. *Nature* **461**, 772-775 (2009).
25. Hafezi, M., Demler, E. A., Lukin, M. D. & Taylor, J. M. Robust optical delay lines with topological protection. *Nat. Phys.* **7**, 907-912 (2011).
26. Poo, Y., Wu, R. X., Lin, Z. F., Yang, Y. & Chan, C. T. Experimental Realization of Self-Guiding Unidirectional Electromagnetic Edge States. *Phys. Rev. Lett.* **106**, 093903 (2011).
27. Fang, K. J., Yu, Z. F. & Fan, S. H. Realizing effective magnetic field for photons by controlling the phase of dynamic modulation. *Nat. Photonics* **6**, 782-787 (2012).
28. Khanikaev, A. B. *et al.* Photonic topological insulators. *Nat. Mater.* **12**, 233-239 (2013).
29. Rechtsman, M. C. *et al.* Photonic Floquet topological insulators. *Nature* **496**, 196-200 (2013).
30. Chen, W. J. *et al.* Experimental realization of photonic topological insulator in a uniaxial metacrystal waveguide. *Nat. Commun* **5**, 5782 (2014).
31. Wu, L. H. & Hu, X. Scheme for Achieving a Topological Photonic Crystal by Using Dielectric Material. *Phys. Rev. Lett.* **114**, 223901 (2015).

32. Cheng, X. J. *et al.* Robust reconfigurable electromagnetic pathways within a photonic topological insulator. *Nat. Mater.* **15**, 542-548 (2016).
33. Barik, S. *et al.* A topological quantum optics interface. *Science* **359**, 666-668 (2018).
34. Gorlach, M. A. *et al.* Far-field probing of leaky topological states in all-dielectric metasurfaces. *Nat. Commun.* **9** (2018).
35. Ni, X. *et al.* Spin- and valley-polarized one-way Klein tunneling in photonic topological insulators. *Sci. Adv.* **4**, eaap8802 (2018).
36. Khanikaev, A. B., Fleury, R., Mousavi, S. H. & Alu, A. Topologically robust sound propagation in an angular-momentum-biased graphene-like resonator lattice. *Nat. Commun.* **6**, 8260 (2015).
37. Yang, Z. J. *et al.* Topological Acoustics. *Phys. Rev. Lett.* **114**, 114301 (2015).
38. Fleury, R., Khanikaev, A. B. & Alu, A. Floquet topological insulators for sound. *Nat. Commun.* **7**, 11744 (2016).
39. He, C. *et al.* Acoustic topological insulator and robust one-way sound transport. *Nat. Phys.* **12**, 1124–1129 (2016).
40. Peng, Y. G. *et al.* Experimental demonstration of anomalous Floquet topological insulator for sound. *Nat. Commun.* **7**, 13368 (2016).
41. Lu, J. Y. *et al.* Observation of topological valley transport of sound in sonic crystals. *Nat. Phys.* **13**, 369-374 (2017).
42. Ni, X., Gorlach, M. A., Alu, A. & Khanikaev, A. B. Topological edge states in acoustic Kagome lattices. *New J. Phys.* **19**, 055002 (2017).
43. Ding, Y. J. *et al.* Experimental Demonstration of Acoustic Chern Insulators. *Phys. Rev. Lett.* **122** (2019).
44. Mukherjee, S. et al. Experimental observation of anomalous topological edge modes in a slowly driven photonic lattice. *Nat. Commun.* **8**, 13918 (2017).
45. Maczewsky, L. *et al.* Observation of photonic anomalous Floquet topological insulators. *Nat. Commun.* **8**, 13756 (2017).
46. Maczewsky, L.J., Höckendorf, B., Kremer, M. et al. Fermionic time-reversal symmetry in a photonic topological insulator. *Nat. Mater.* **19**, 855–860 (2020).
47. Tymchenko, M. & Alu, A. Circuit-Based Magnetless Floquet Topological Insulator. *Int. Congress on Adv. Electromagnetic Materials in Microw. and Optics (Metamaterials)*, 373-375 (2016).
48. Darabi, A., Ni, X., Leamy, M. & Alu, A. Reconfigurable Floquet elastodynamic topological insulator based on synthetic angular momentum bias. *Sci. Adv.* **6**, eaba8656, (2020).
49. Hu, W. *et al.* Measurement of a topological edge invariant in a microwave network. *Phys. Rev. X* **5**, 011012 (2015).
50. Gao, F. *et al.* Probing topological protection using a designer surface plasmon structure. *Nat. Commun.* **7**, 11619 (2016).
51. Wintersperger, K. *et al.* Realization of an anomalous Floquet topological system with ultracold atoms. *Nat. Phys.* **16**, 1058–1063 (2020).
52. Nagulu, A., Tymchenko, M., Alù, A. & Krishnaswamy, H. Ultra Compact, Ultra Wideband, DC-1GHz CMOS Circulator Based on Quasi-Electrostatic Wave Propagation in Commutated Switched Capacitor Networks. IEEE *Radio Freq. Integ. Circuits Symp. (RFIC)* (2020).

53. Tymchenko, M., Sounas, D., Nagulu, A., Krishnaswamy, H. and Alù, A. Quasielectrostatic wave propagation beyond the delay-bandwidth limit in switched networks. *Phys. Rev. X*, **9**, 031015, 2019.
54. Estep, N. A., Sounas, D. L., Soric, J. & Alu, A. Magnetic-free non-reciprocity and isolation based on parametrically modulated coupled-resonator loops. *Nat. Phys.* **10**, 923–927 (2014).
55. Lathi, B.P., 1998. *Modern Digital and Analog Communication Systems 3e Osece*. Oxford University Press, Inc.
56. Reiskarimian, N. & Krishnaswamy, H. Magnetic-free non-reciprocity based on staggered commutation. *Nat. Commun. 7*, 11217 (2016).
57. Chalker, J. T. & Coddington, P. D. Percolation, Quantum Tunnelling and the Integer Hall-Effect. *J. Phys. C Solid State* **21**, 2665-2679 (1988).
58. Liang, G. Q. & Chong, Y. D. Optical Resonator Analog of a Two-Dimensional Topological Insulator. *Phys. Rev. Lett.* **110** (2013).
59. Pasek, M. & Chong, Y. D. Network models of photonic Floquet topological insulators. *Phys. Rev. B* **89** (2014).
60. Delplace, P., Fruchart, M., & Tauber. C. Phase rotation symmetry and the topology of oriented scattering network. *Phys. Rev. B* **95**, 205413 (2017).
61. Skirlo, S. A., Lu, L., Igarashi, Y., Yan, Q., Joannopoulos, J. & Soljačić, M. Experimental Observation of Large Chern Numbers in Photonic Crystals. *Phys. Rev. Lett.* **115**, 253901 (2015).
62. Bharadia, D., McMilin, E. & Katti, S. Full duplex radios. *Proceedings of the ACM SIGCOMM*, 375–386 (2013).
63. Zhou, J. et al. Integrated full duplex radios. *IEEE Commun. Mag.* **55**, 142–151 (2017).
64. Katanbaf, M., Chu, K., Zhang, T., Su, C. & Rudell, J. C. Two-Way Traffic Ahead: RF/Analog Self-Interference Cancellation Techniques and the Challenges for Future Integrated Full-Duplex Transceivers. IEEE *Microwave Magazine* **20**, 22-35 (2019).
65. Nagulu, A. & Krishnaswamy, H. Non-magnetic CMOS switched-transmission-line circulators with high power handling and antenna balancing: Theory and implementation. IEEE *J. Solid-State Circuits* **54**, 1288-1303 (2019).
66. Dinc, T. et al. Synchronized conductivity modulation to realize broadband lossless magnetic-free non-reciprocity. *Nat. Commun.* **8**, 795 (2017).
67. Dastjerdi, M. B., Reiskarimian, N., Chen, T., Zussman, G. & Krishnaswamy, H. Full Duplex Circulator-Receiver Phased Array Employing Self-Interference Cancellation via Beamforming. IEEE *Radio Freq. Integ. Circuits Symp. (RFIC)*, 108-111 (2018).
68. Dastjerdi, M. B., Jain, S., Reiskarimian, N., Natarajan, A. & Krishnaswamy, H. Analysis and Design of a Full-Duplex Two-Element MIMO Circulator-Receiver With High TX Power Handling Exploiting MIMO RF and Shared-Delay Baseband Self-Interference Cancellation. IEEE *J. Solid-State Circuits* **54**, 3525-3540 (2019).
69. Immoreev, I. & Fedotov, D. V. Ultra wideband radar systems: advantages and disadvantages. IEEE *Conf. Ultra Wideband Systems and Tech. (UWBWST)*, 201–205 (2002).

70. Roderick, J., Krishnaswamy, H., Newton, K. & Hashemi, H. Silicon-Based Ultra-Wideband Beam-Forming. IEEE *J. Solid-State Circuits* **41**, 1726-1739 (2006).
71. Chu, T., Roderick, J. & Hashemi, H. An Integrated Ultra-Wideband Timed Array Receiver in 0.13 μm CMOS Using a Path-Sharing True Time Delay Architecture. IEEE *J. Solid-State Circuits* **42**, 2834-2850 (2007).
72. Rajesh, N. & Pavan, S. Design of Lumped-Component Programmable Delay Elements for Ultra-Wideband Beamforming. IEEE *J. of Solid-State Circuits* **49**, 1800-1814 (2014).
73. Mondal, I. & Krishnapura, N. A 2-GHz Bandwidth, 0.25–1.7 ns True-Time-Delay Element Using a Variable-Order All-Pass Filter Architecture in 0.13 μm CMOS. IEEE *J. of Solid-State Circuits* **52**, 2180-2193 (2017).

Figures

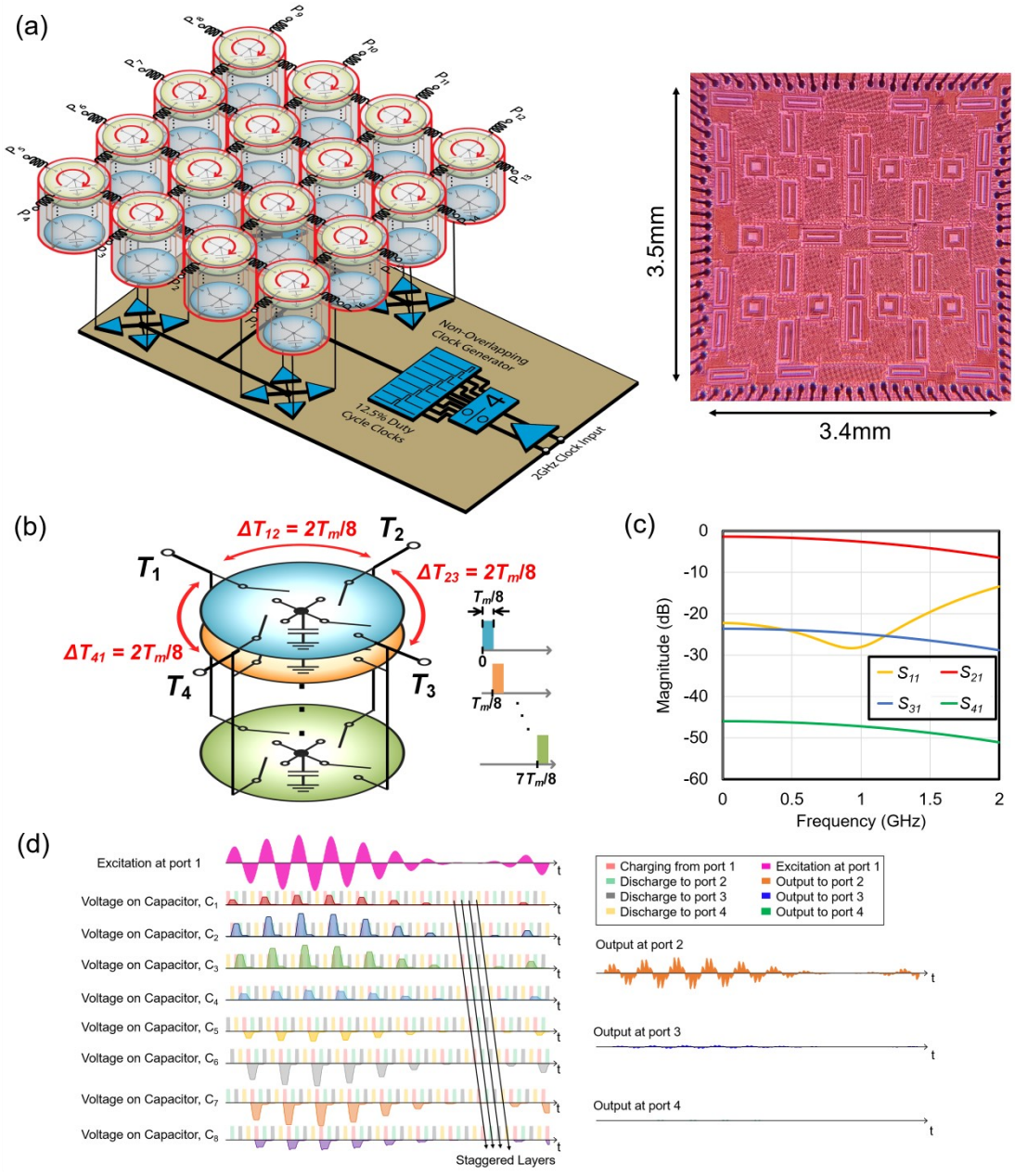

Figure 1: (a) Conceptual diagram and chip microphotograph of the 4×4 dispersion-free quasi-electrostatic Floquet TI implemented in a 45nm SOI CMOS process. (b) Circuit and timing diagram, (c) simulated scattering parameters, and (d) time-domain operation of a 4-port, 8-layer synthetically-helicoidally-rotating quasi-electrostatic circulator modulated at f_m=500MHz with shunt capacitors C=2.5pF and matching inductors L=2.5nH at the ports, exhibiting low-loss transmission and high isolation across a wide bandwidth.

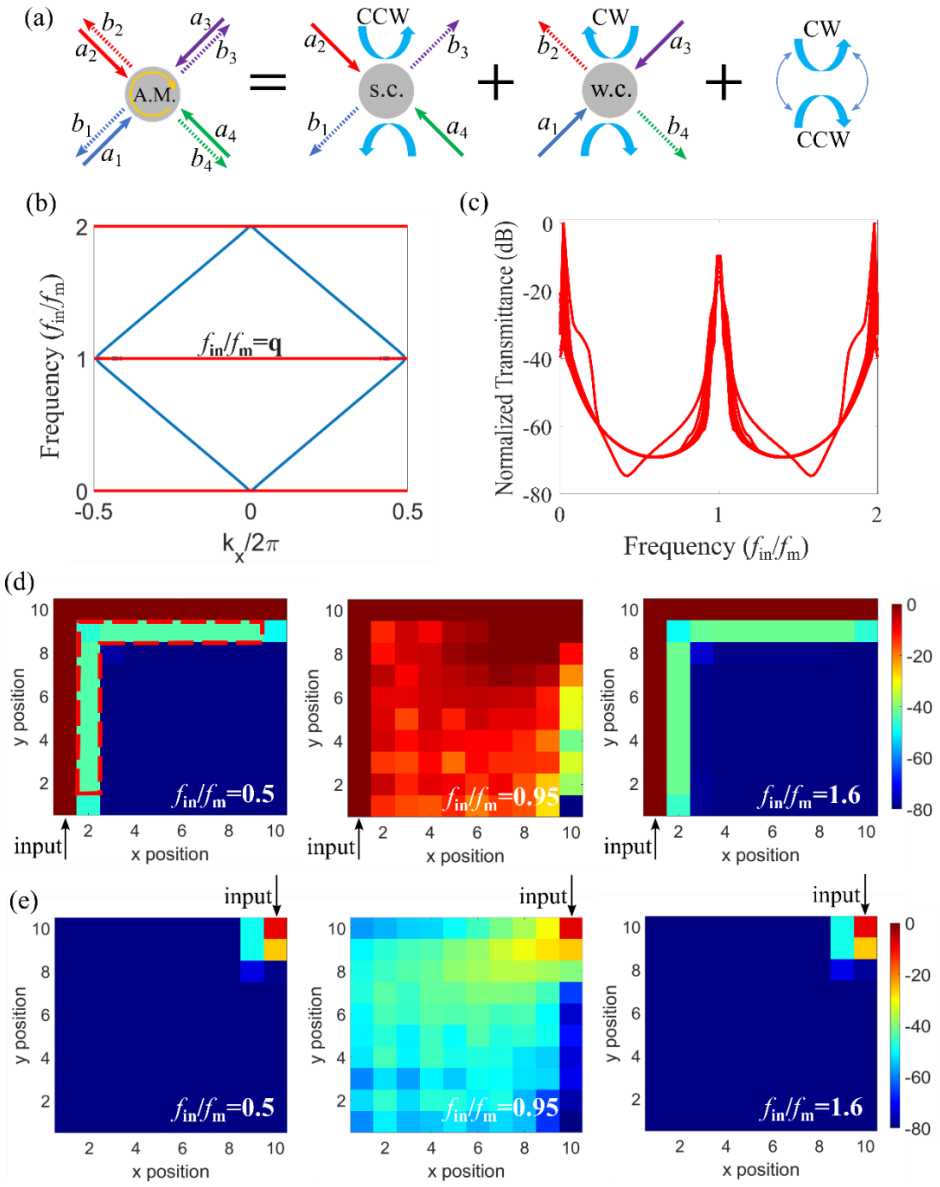

Figure 2: Floquet TI based on resonator-free network: (a) schematic relation between the scattering processes of a 4-port scatterer and those of 2-port scatterers, and (b) band structure of a supercell network formed by the four-port circulators, which consists of 10 unit cells in the y direction. Bloch periodic boundaries are applied in the x direction. Red lines represent the flat bulk bands, and blues lines represent the topological edge states which are continuously extended in frequency. (c) Transmittance spectra of the bulk, which are calculated from the data taken at sites next to the edges, indicated by the dashed red lines in the left panel of (d). (d,e) Normalized field distribution of a finite network consisting of 10×10 *elements when the input port is placed at (d) the left bottom site, and (e) the right top site. Continuous boundary conditions are applied at the upper and left edges of the lattice, and zero boundary conditions are applied at the bottom and right edges.*

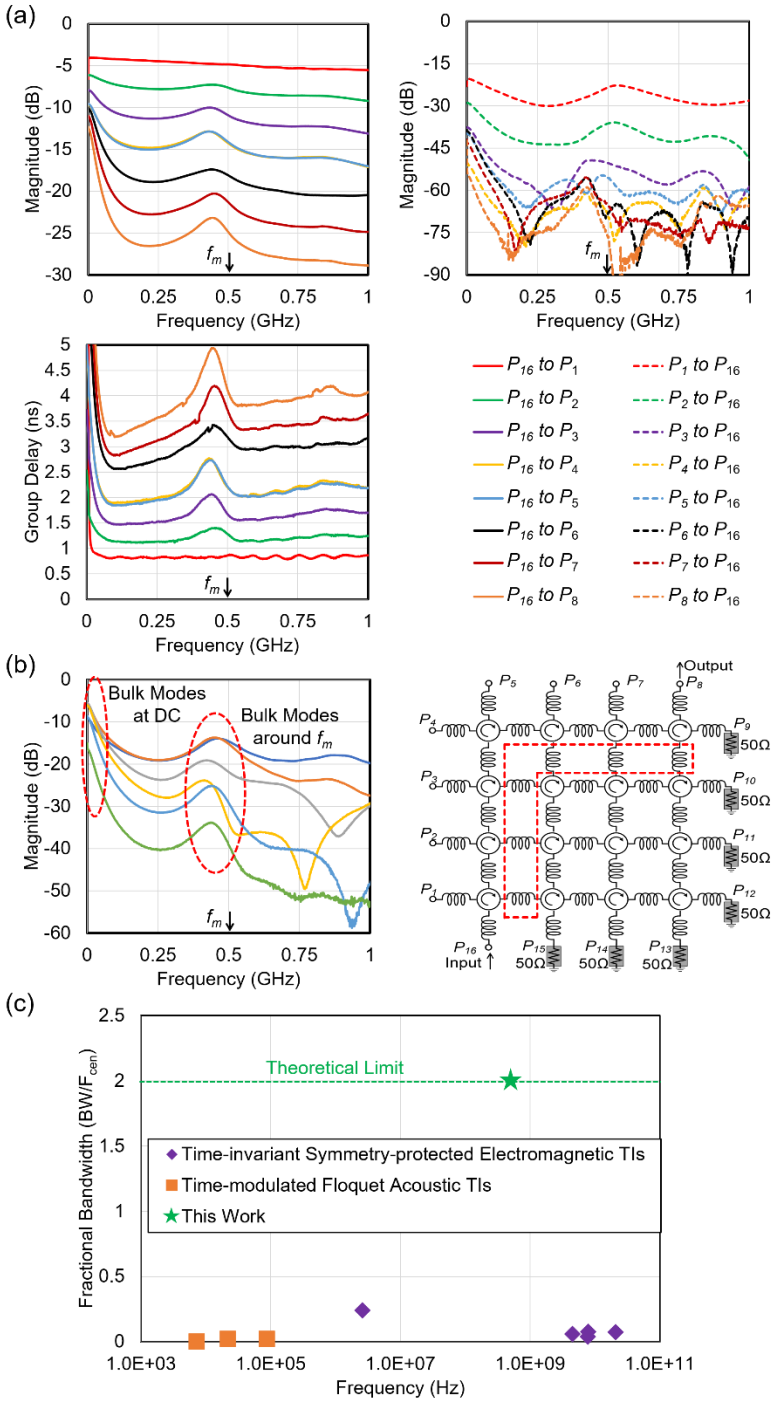

Figure 3: (a) Measured CW transmission, CCW isolation and CW group delay parameters at the edge nodes (from P1 to P8) when all the unit cells are configured for CW propagation. (b) Measured transmission at the bulk nodes which are one site away from the edge as marked using the red dashed line in the 4×4 lattice on the right . (c) Fractional

bandwidths of several prior time-invariant symmetry-protected electromagnetic TIs, time-modulated acoustic TIs and our quasi-electrostatic chip-scale Floquet TI across their operating center frequency.

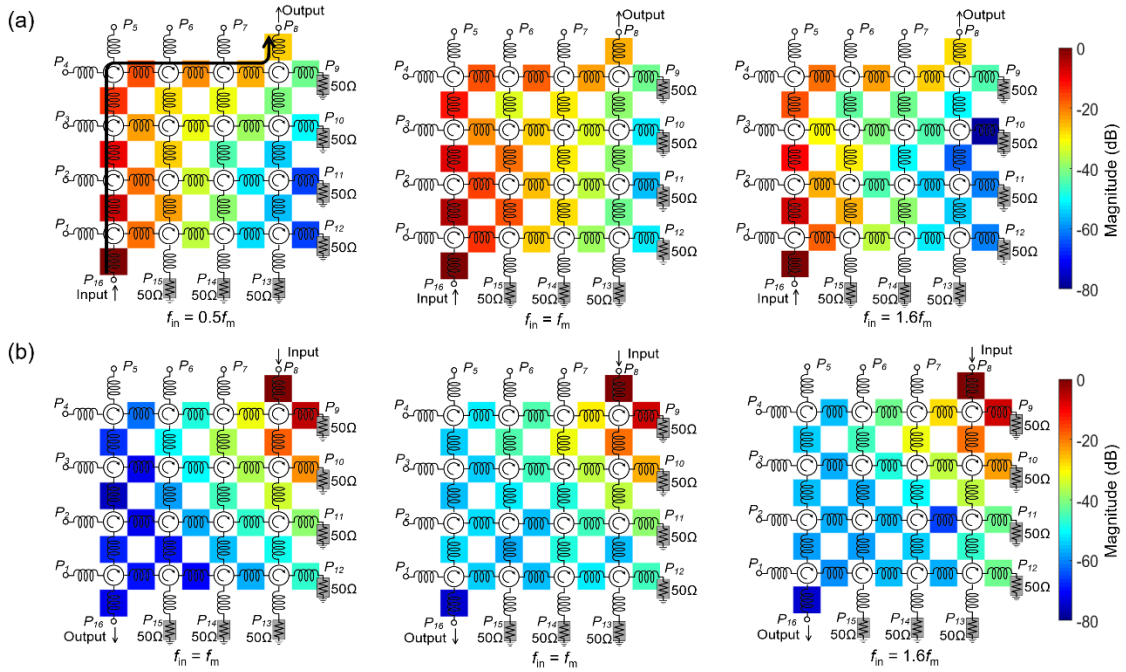

Figure 4: (a) and (b) Measured field distributions in dB scale of the signal traveling through the lattice across a wide frequency range when traveling in-line with the lattice topology (CW direction, P_{16} to P_8) and in opposite direction of the lattice topology (CCW direction, P_8 to P_{16})

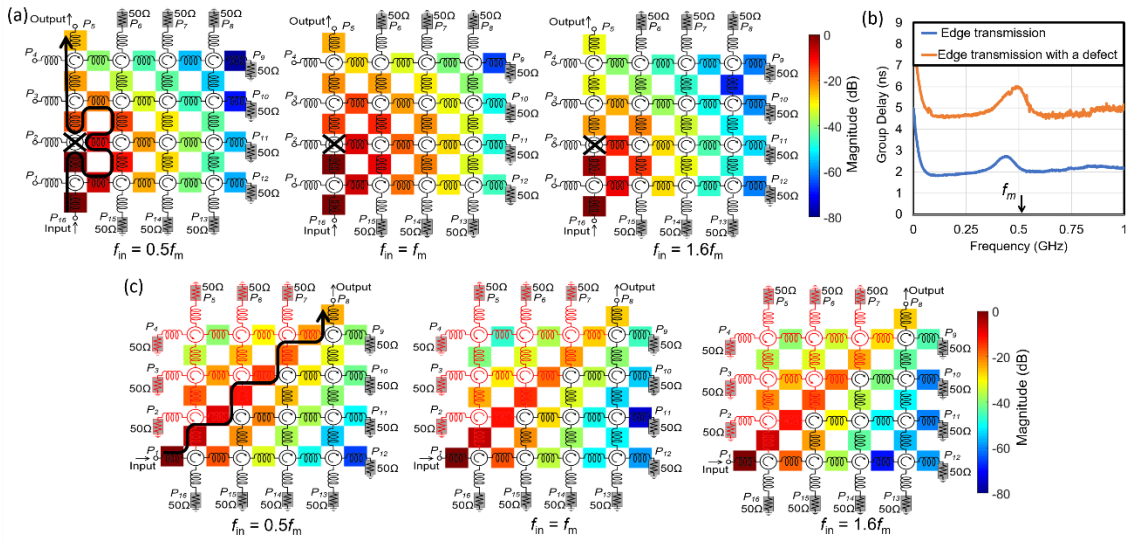

Figure 5: (a) Measured field distribution of the signal traveling along the edge mode in the presence of an artificially induced defect by turning OFF a unit cell along the edge. (b) Transmission group delays with and without the artificially induced defect, showing the longer path taken by the signal around the defect. (c) Measured field distributions of the signal traveling along the domain wall created by choosing different handedness for the unit cells on either side of the domain wall.

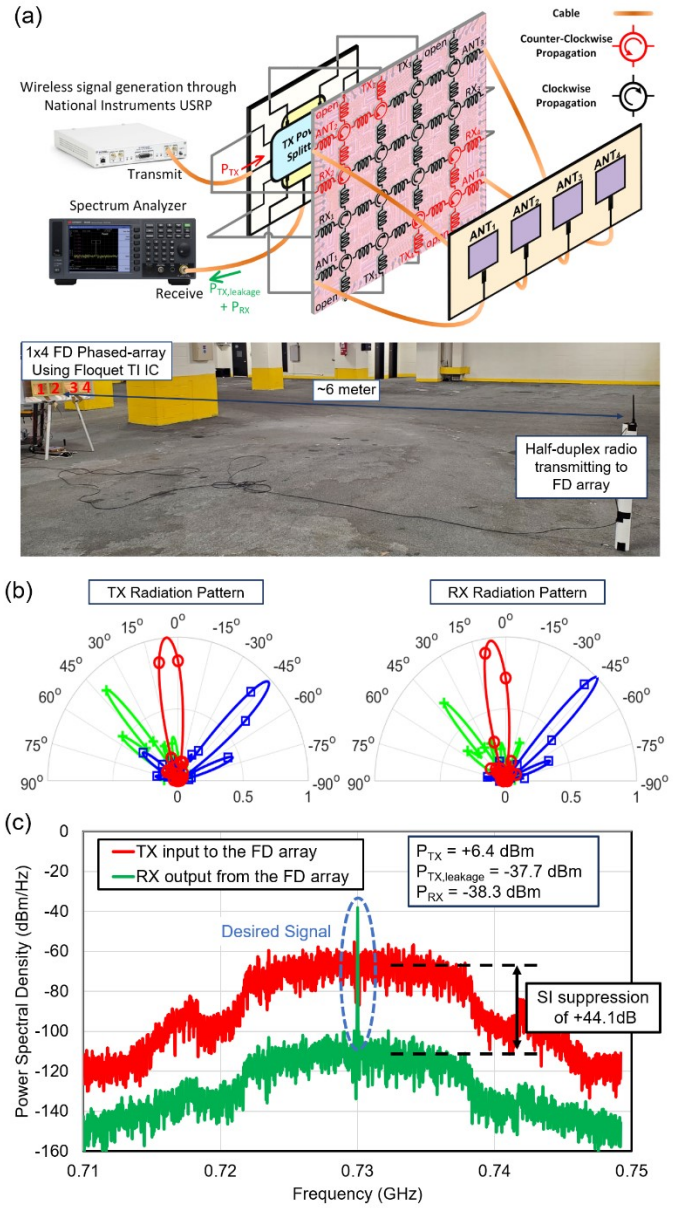

Figure 6: (a) Experimental setup and wireless demonstration of a 4-element 730MHz full-duplex phased array where 4 transmitters, receivers and antennas are interfaced through our reconfigurable CMOS Floquet-TI IC. (b) Transmitter and receiver beam-steering performance obtained by leveraging the programmable delays provided by the Floquet TI lattice. Each color depicts an array radiation pattern steered towards a different angle of transmission/reception, namely -45º (blue),0º (red) and 45º (green). (c) Measured desired signal and transmitter self-interference when the transmitter and receiver arrays are steered to +45º and 0º respectively. When transmitting a 20MHz, OFDM-QPSK signal with a total transmit power of +6.4dBm, we measured an array self-interference suppression of

+44.1dB, enabling the simultaneous reception of a +10dBm continuous-wave signal transmitted from a dipole antenna 6m away with ~0dB SINR.

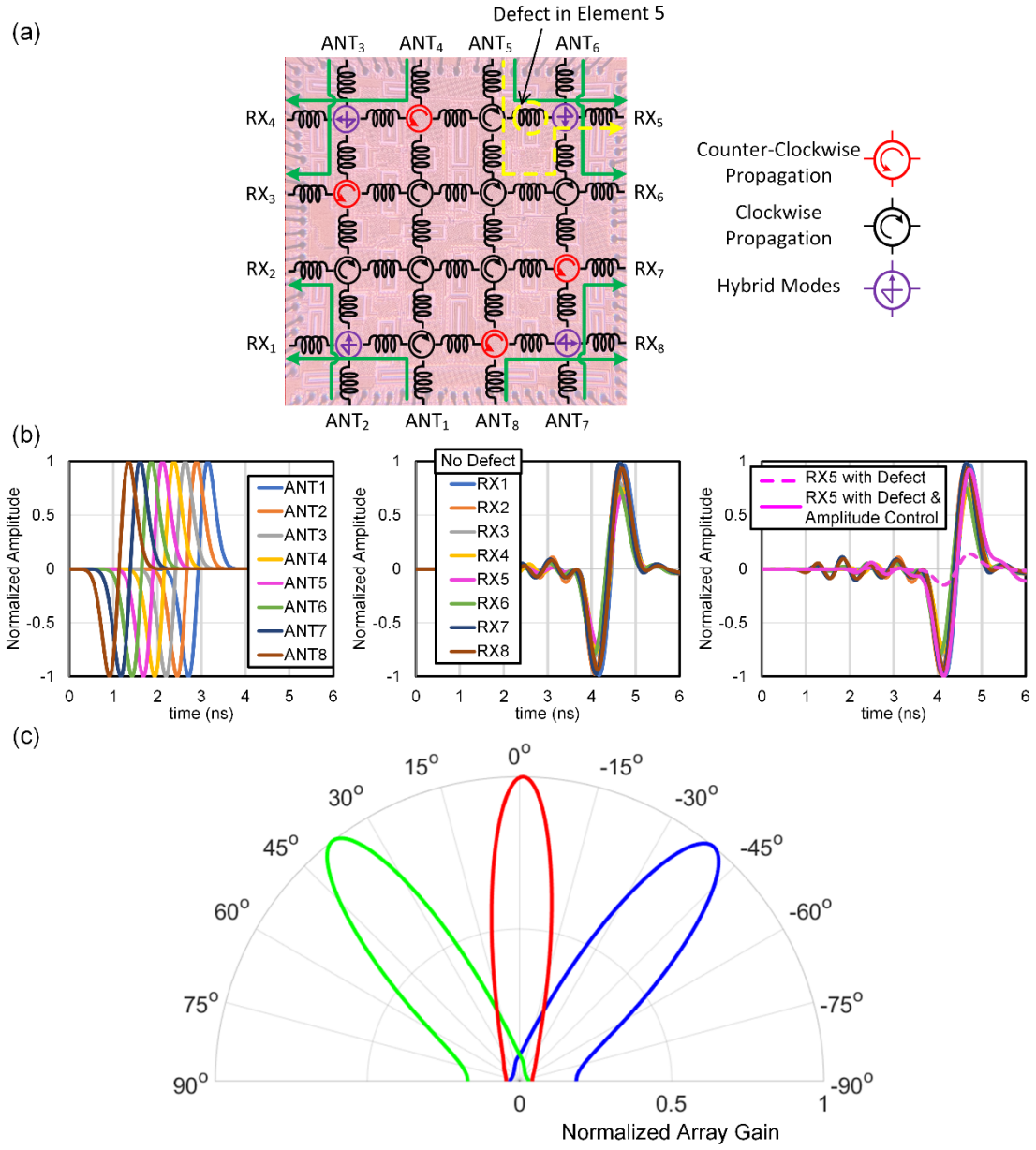

Figure 7: (a) Configuration diagram of the Floquet TI lattice when programmed for wideband, true-time delay beamforming between 8 receiver ports and 8 antenna ports connected to a 1×8 antenna array. Green and yellow paths depict the signal paths with and without a defect which is artificially induced by turning off the switches in the 5th beamforming path. (b) Time domain simulation for an 8-element array with antenna spacing of 12cm using measured scattering parameters of the Floquet TI. Time-shifted

Gaussian mono-pulse waveforms with a carrier frequency of 730MHz and a -3dB bandwidth of 860MHz are incident at the antenna ports to emulate an excitation at -40^o angle of arrival. In presence of an artificially induced defect, the signal travels around it, preserving the signal propagation and beamforming capabilities. Adjusting the delays in the unit cells enables achieving the desired delay despite the longer transmission path. A longer path can lead to higher transmission loss which can be easily compensated through amplitude/gain control, which is straightforward to implement in beamformers. (c) Synthesized wideband beam patterns provided by the Floquet TI (sans the defect) when the programmable delays are configured for normal, +40^o and -40^o steering.